A&A 672, L14 (2023)
https://doi.org/10.1051/0004-6361/202245184


Astronomy & Astrophysics

LETTER TO THE EDITOR

# A redshifted excess in the broad emission lines after the flare of the $\gamma$-ray narrow-line Seyfert 1 PKS 2004−447

W. Hon[1,2], M. Berton[1], E. Sani[1], R. Webster[2], C. Wolf[3,4], A. F. Rojas[5,6], P. Marziani[7], J. Kotilainen[8,9], and E. Congiu[10,1]

[1] European Southern Observatory, Alonso de Córdova 3107, Casilla 19, Santiago 19001, Chile
e-mail: whon@student.unimelb.edu.au
[2] School of Physics, University of Melbourne, Parkville, Victoria 3010, Australia
[3] Research School of Astronomy and Astrophysics, Australian National University, Canberra, ACT 2611, Australia
[4] Centre for Gravitational Astrophysics, Australian National University, Canberra, ACT 2611, Australia
[5] Centro de Astronomía (CITEVA), Universidad de Antofagasta, Avenida Angamos 601, Antofagasta, Chile
[6] Núcleo de Astronomía de la Facultad de Ingeniería, Universidad Diego Portales, Av. Ejército Libertador 441, Santiago 22, Chile
[7] INAF – Osservatorio Astronomico di Padova, Vicolo dell'Osservatorio 5, 35122 Padova, Italy
[8] Finnish Centre for Astronomy with ESO (FINCA), University of Turku, Quantum, Vesilinnantie 5, 20014 Turku, Finland
[9] Department of Physics and Astronomy, University of Turku, Quantum, Vesilinnantie 5, 20014 Turku, Finland
[10] Departamento de Astronomía, Universidad de Chile, Camino del Observatorio 1515, Las Condes, Santiago, Chile

Received 11 October 2022 / Accepted 20 March 2023

**ABSTRACT**

PKS 2004−447 is a narrow-line Seyfert 1 (NLS1) harbouring a relativistic jet with $\gamma$-ray emission. On 2019 October 25, the *Fermi*-Large Area Telescope captured a $\gamma$-ray flare from this source, offering a chance to study the broad-line region (BLR) and jet during such violent events. This can provide insights into the BLR structure and jet interactions, which are important for active galactic nuclei (AGN) and host galaxy co-evolution. We report X-shooter observations of enhancements in the broad line components of Balmer, Paschen, and He I lines seen only during the post-flare and vanishing 1.5 years after. These features are biased redwards up to ∼250 km s$^{-1}$ and are narrower than the pre-existing broad line profiles. This indicates a connection between the relativistic jet and the BLR of a young AGN, and how $\gamma$-ray production can lead to localised addition of broad emission lines.

**Key words.** galaxies: active – galaxies: jets – galaxies: nuclei – galaxies: Seyfert – quasars: emission lines

## 1. Introduction

Since the first observations (Seyfert 1943) of broad features in active galactic nuclei (AGN) spectra, the nature of the emitting region in terms of its motions and structure has been the subject of much discussion and speculation (e.g., Mathews & Capriotti 1985; Leighly & Casebeer 2007; Bon et al. 2009; Shapovalova et al. 2009; Yong et al. 2017). The general view of the broad-line region (BLR) is that it is a region of photoionised gas that is subjected to high velocities – with a full width at half maximum (FWHM) > 2000 km s$^{-1}$ – through random dispersion and/or virialised orbital rotational motions, as well as having a potential for bulk infall or outflow (e.g., Wanders et al. 1995; Done & Krolik 1996; Denney et al. 2009; Williams et al. 2018).

Broad-line-region outflows are of particular interest to the topic of AGN and host galaxy co-evolution (Zubovas & Nayakshin 2014; King & Pounds 2015; Harrison et al. 2018). In addition to cases of blue-shifted emission lines (e.g., Ge et al. 2019), broad absorption lines are observed in ∼20% of quasars (Hamann et al. 1993; Trump et al. 2006), and can reach velocities up to $v \sim 0.3c$ (Rogerson et al. 2016; Choi et al. 2020). This is sufficient energy (Scannapieco & Oh 2004; Hopkins & Elvis 2010; Harrison et al. 2018) to effectively cause feedback to the host galaxy as it eventually reaches and interacts with the interstellar medium.

Narrow-line Seyfert 1 (NLS1) galaxies are mainly characterised by broad emission lines that are observed to be narrower than typical AGN ($FWHM < 2000$ km s$^{-1}$). They also show strong Fe II multiplet emissions and a low flux ratio [O III]/H$\beta$ < 3 (see Komossa 2008, for an in-depth review). NLS1s harbour low-mass supermassive black holes of $10^6$–$10^8$ $M_\odot$ and are considered early stage AGN (Boller et al. 1996; Peterson et al. 2000; Cracco et al. 2016; Rakshit et al. 2017; Chen et al. 2018). Roughly ∼7% of them harbour relativistic jets (Mathur 2000; Sulentic et al. 2000; Grupe 2000; Komossa et al. 2006). A few dozen of them have been identified as $\gamma$-ray sources (hereafter $\gamma$-NLS1s) after the launch of the *Fermi*-Large Area Telescope (Abdo et al. 2009; Foschini 2020). Furthermore, $\gamma$-NLS1s have the added properties of superluminal motion, violent variability, and optical polarisation from the relativistic jets (Liu et al. 2010; Itoh et al. 2013; Maune et al. 2012; Paliya et al. 2013). Specifically, they have very similar properties to the beamed jetted AGN sub-class of flat-spectrum radio quasars (FSRQs, Foschini et al. 2015) as they represent the low-mass, low-luminosity, and probably young-age tail of the FSRQs' distribution (Berton et al. 2016, 2017).

PKS 2004−447 (RA 20 h 07 m 55 s, Dec −44 d 34 m 44 s, $z \sim 0.24$), the main focus of this paper, is a $\gamma$-ray NLS1. The source has the spectral energy distribution of beam-jetted AGN (Gallo et al. 2006; Kreikenbohm et al. 2016; Gokus et al. 2021) and is hosted in a face-on, pseudo-bulge spiral galaxy (Kotilainen et al. 2016). The radio morphology of PKS 2004−447 suggests an angle relative to a line of sight of <50 deg (Schulz et al. 2016), similar to the $\gamma$-NLS1, 3C 286 (Berton et al. 2017; An et al. 2017; Yao & Komossa 2021), although different to other sources with <10 deg angles (e.g., D'Ammando et al. 2013; Lister et al. 2016). It is less variable in X-rays and radio when compared to other $\gamma$-NLS1s (e.g., see PMN J0948+0022, Foschini et al. 2012). Most importantly, the source underwent a $\gamma$-ray flare that was detected by the *Fermi*-Large Area Telescope on 2019 October 25, which represents an ideal laboratory to study possible effects of the jet over the BLR.

In this work, we present a detailed analysis of the broad emission lines of X-shooter data of PKS 2004−447 surrounding the $\gamma$-ray flare. There are two 'low-state' spectra taken on 2017 May 28 (SP0) and 2017 June 19 (SP1, both in programme 099.B-0785). After the flare, a 'post-flare' spectrum was obtained on 2019 November 25 (SP2), and then a 'reverted-state' spectrum on 2021 May 05 (SP3, both in Director Discretionary Time programme 104.20UC). We deliberately observed the post-flare spectrum, SP2, when the $\gamma$-ray flare was predicted to reach the BLR (see Berton et al. 2021, for size estimations). We show, for the very first time, a temporal relation between a $\gamma$-ray event, jet flaring, and BLR changes localised to the redshifted part of the emitting region. This work adopts a standard ΛCDM cosmology with $H_0 = 70\,\mathrm{km\,s^{-1}\,Mpc^{-1}}$ and $\Omega_\lambda = 0.7$. All magnitudes are provided in the AB system.

## 2. X-shooter observations and data reductions

X-shooter observes simultaneously in the UVB, VIS, and NIR arms, spanning a total wavelength range of 3000–25 000 Å. All four spectra were taken with a 1″ slit. Details of the four X-shooter spectra are listed in Table 1, and they are displayed over the full X-shooter range in the appendix (see Fig. A.2).

For the reduction of raw data, we used the default X-shooter pipeline provided by ESO[1] with bias, flat, lamp corrections, and response correction with a standard star. We also used ESO Molecfit[2] to remove the telluric absorptions (Smette et al. 2015; Kausch et al. 2015). SP1 had sufficient signal in the NIR arm of X-shooter to accurately recover the features and the continuum that was absorbed. We de-reddened the spectra using a Fitzpatrick (1999) law with $E(B-V) = 0.0846$ (Schlafly & Finkbeiner 2011) and $R_v = 3.1$. We measured the Na I doublet to obtain the redshift of the host galaxy, obtaining a value of $z = 0.24035 \pm 0.00009$ for SP0, SP1, and SP3, and $z = 0.24050 \pm 0.00009$ for SP2 due to the motion of the Earth. We assume the lower value redshift for calculations in this work, and an operating rest-frame wavelength of 2418–20 155 Å.

The airmasses and seeing vary for the four observations, suggesting a need to fine-tune flux calibration. This is usually done by assuming non-varying forbidden lines, but the different slit orientations sample different parts of the narrow-line region. This variation only affects the forbidden-line, as the continuum and permitted lines from the central region are well within the 1″ slit. Thus, the flux per spectrum was fine-tuned based on the acquisition images (details in Appendix A). The calibration is accurate as the spectra match the spectral energy distribution (SED) from Gokus et al. (2021) in Fig. 1. It is not possible to compare the variation in the forbidden lines across these four spectra due to this systematic.

By averaging SP0, SP1, and SP3, we constructed SP013, a higher signal-to-noise ratio (S/N) stacked spectrum representing the long-term average of PKS 2004−447. This smooths out stochastic and systematic variation that is not characterised, and serves as the baseline for comparing with SP2. Statistically significant residuals in SP2−SP013 can be easily attributed to the $\gamma$-ray flare.

## 3. Results

The continuum of PKS 2004−447 is blended. There is the power law from the AGN accretion disk; Fe II multiplet emission; a host galaxy that is resolved in the aperture (Kreikenbohm et al. 2016); and synchrotron emission from the jet. Its UV-NIR frequencies are dominated by synchrotron emission, resulting in a negative slope instead of the usual positive power law (Gokus et al. 2021). During the flare, the flux is boosted across all X-shooter wavelengths, with a greater increase for lower frequencies.

To characterise the differences between the four datasets, we constructed root mean square (rms) spectra using Eq. (3) from Peterson et al. (2004). Figure 2 shows the rms spectra with and without SP2. Without SP2, no features appear above the noise around H$\delta$, H$\gamma$, H$\beta$, and He I$\lambda$5875. With SP2, those lines show noticeable enhancements. We investigated each spectrum's variability relative to SP013 and we find that the enhancement only appears in SP2, suggesting that the broad emission lines in the Balmer and helium series changed temporarily in SP2, likely related to the $\gamma$-ray flare.

We can also see the effects of mismatched slit orientations here. While SP1−SP013 has somewhat clean subtractions in the forbidden lines, SP0−SP013 and SP3−SP013 do not. This makes interpreting the changes in H$\alpha$ difficult. While this emission line is also affected, it is hard to disentangle observed and systematic variation on the [N II] line.

A closer look at the enhancement in H$\beta$ as well as a comparison of all epochs can be found in Fig. 3 (see Fig. B.2 for the full version). Outside of SP2, the H$\beta$ line remains constant with the subtracted spectrum, consistent with a ∼0 mean value within the noise level. All of the H$\beta$ enhancement is significant[3] at >6$\sigma$. We also discover that the peak of the H$\beta$ excess is redshifted by[4] 240±50 km s$^{-1}$ (4.8$\sigma$), which is consistent across all of the subtracted spectrum. We refer to this enhancement with a redward bias as the 'red excess'. All of the Balmer lines and He I$\lambda$10830 exhibit the red excess, but it is less obvious in He I$\lambda$5875 (see Fig. B.2). Weaker enhancements are seen in Pa$\beta$ and Pa$\alpha$; however, they are not significantly redshifted. Also O I and Mg II have no enhancements.

Line fitting is not trivial for PKS 2004−447 as the continuum is not a power law. Approximations can work for individual epochs, but they are inconsistent across all four spectra. This is because both the emission lines and continuum can vary, so it is

[1] https://www.eso.org/sci/software/pipelines/index.html#reflex_workflows

[2] Molecfit Pipeline Team, MOLECFIT Pipeline User Manual, 2021. ESO VLT-MAN-ESO-19550-5772.

[3] Calculated with the peak flux value of the enhancement and the rms of the SP2 continuum. The window for rms is 5300–5400 Å the same as used in S/N calculation in Table 1.

[4] Error quoted here accounts for line fitting uncertainty and X-shooter resolution of 35 km s$^{-1}$ at H$\beta$.

**Table 1.** X-shooter observations.

| Name | Epoch (Date) | Epoch (MJD) | Airmass start | Airmass end | Seeing | Exposure time (s) | Rotation (°) | $S/N$ | SDSS $r$ (AB mag) |
|---|---|---|---|---|---|---|---|---|---|
| SP0 | 2017-05-28 | 57901.206 | 1.453 | 1.231 | 1.05 | 235 | 0 | 13 | 18.448 |
| SP1 | 2017-06-19 | 57923.214 | 1.156 | 1.080 | 1.21 | 235 | 40 | 13 | 18.457 |
| SP2 | 2019-11-25 | 58812.027 | 1.636 | 2.106 | 1.27 | 750 | 10 | 24 | 18.188 |
| SP3 | 2021-05-05 | 59339.368 | 1.096 | 1.065 | 0.94 | 750 | 50 | 17 | 18.528 |

**Notes.** Columns: (1) spectrum name; (2) observation date; (3) observation date in modified Julian date (MJD); (4) airmass at the beginning of the observation; (5) airmass at the end of the observation; (6) DIMM seeing during the observation; (7) exposure time in seconds; (8) slit rotation as measured with respect to the first spectrum, SP0; (9) signal-to-noise ratio measured from the featureless region between 5300–5400 Å; (10) SDSS magnitudes obtained from the flux calibrated acquisition images.

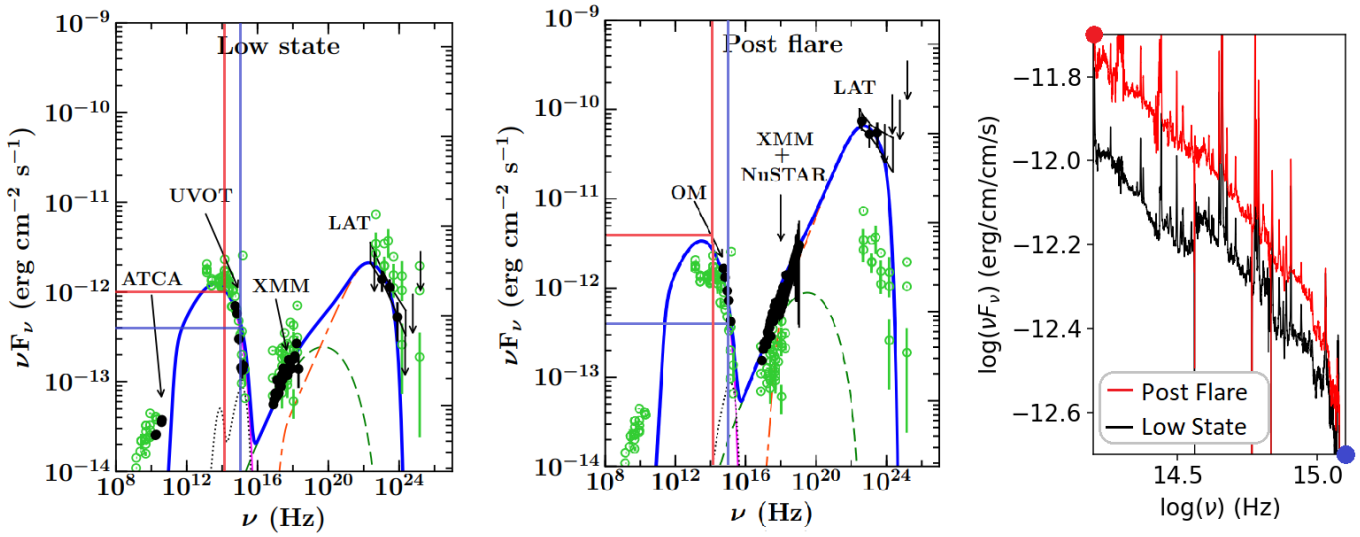


**Fig. 1.** Comparision of the spectral energy distribution of PKS 2004−447 to the photometrically calibrated X shooter spectra. Left and middle panels are adopted from Fig. 6 of Gokus et al. (2021), refer to original paper for detailed legend. Right panel shows SP0, the low state in black, and SP2, the post-flare in red. All three plots have the same axes units. The red and blue horizontal and vertical lines in the left and middle panel indicates the $y$- and $x$-axis limit plotted in the right panel. The match between the SED and spectrum for both states are very close.

not possible to disentangle the source of any measured variation. Therefore, we only fitted SP013 to provide average BLR properties and SP2−SP013 to estimate red excess properties (details in Appendix B). Enhancements and red excesses are present independently and they are not due to continuum modelling.

The width of all lines are around $FWHM = 1600\,\mathrm{km\,s^{-1}}$. All Balmer and Paschen lines have a $<50\,\mathrm{km\,s^{-1}}$ velocity offset, while all He I lines are blueshifted to $85\,\mathrm{km\,s^{-1}}$. In addition, O I$\lambda$8446 is redshifted to $180\,\mathrm{km\,s^{-1}}$, suggesting an inflow.

For the red excess, we measured a $FWHM \sim 1000\,\mathrm{km\,s^{-1}}$ for all Balmer and Paschen lines, but the offset differs for different line series. Furthermore, H$\delta$, H$\gamma$, and H$\beta$ are redshifted by $\sim$250 $\mathrm{km\,s^{-1}}$, and H$\alpha$ is redshifted by $180\,\mathrm{km\,s^{-1}}$. Also He I red excesses are comparatively weaker for this analysis, but we observe roughly the same width and up to $340\,\mathrm{km\,s^{-1}}$ of redshift. As mentioned, Paschen lines do not have a noticeable redshift, suggesting that the red excess is more prominent towards the blue.

## 4. Discussion and conclusion

### 4.1. The impact of observational effects on our findings

We explore the possibility that the red excesses are caused by observational effects. This is a possibility since the observing conditions between all spectra are different. Namely, SP2, which is the spectrum closest to the flare and the spectrum that is showing the red excess, was observed under the worse conditions relative to the rest (see Table 1).

The immediate cause of concern with SP2 is flux dimming caused by high ending airmass at ~2.1 and seeing 1.2″. The drop in flux caused by poor seeing or field differential dispersion is uniform, and this was corrected when we calibrated the flux photometrically (see Appendix A). Also, as seen in Table 1, SP0 and SP1 have a similar S/N given similar exposure times, followed by SP3 and SP2 with the best S/N since PKS 2004−447 is at its brightest. This demonstrates that the quality of spectra is more dependant on exposure times and source brightness.

Moreover, PKS 2004−447 has a scale of 3.8 kpc/″at $z = 0.24$. For a BLR radius of 15 light days (Berton et al. 2021), this corresponds to a diameter of $2.5\times10^{-5}$ kpc, which covers $\ll1''$. With a slit of 1″, this BLR scale is too small for airmass and seeing to have any relevant effect on the emission lines. Even if they did, that should cause the BLR to be dimmer, not brighter, and that would also affect the NLR and Mg II line, which is not observed.

Finally, VLT/X-shooter is equipped with atmospheric differential correctors (ADCs), which prevent spectral distortions for airmass lower than 2.5. Therefore, it is unlikely for the red excess to be an observational artefact.

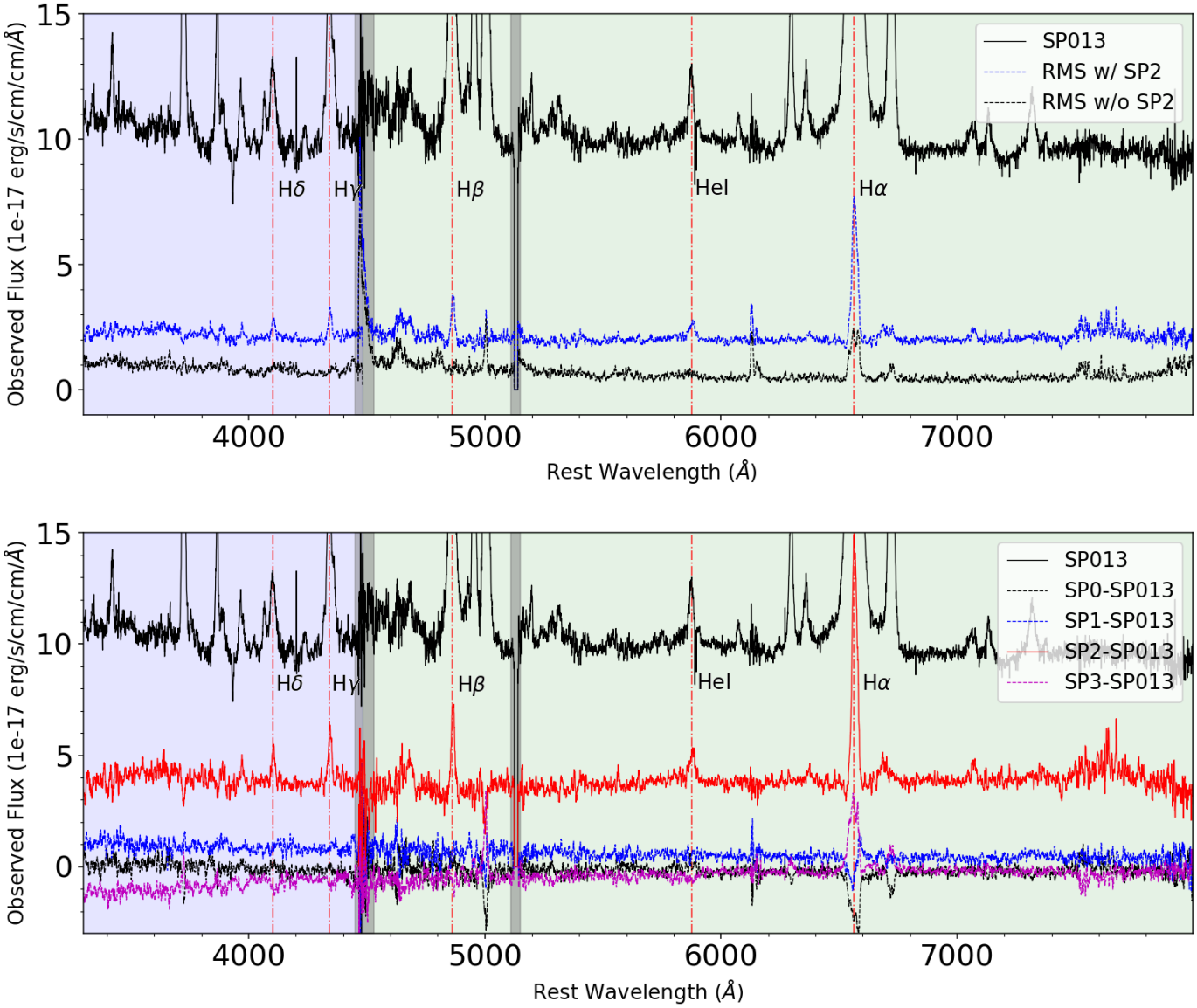


**Fig. 2.** Broad line enhancements in SP2, the post-flare spectrum. All plotted lines are indicated by the respective legends, while vertical dash-dotted line indicates the key Balmer and He I$\lambda$5875 emission line. Blue region represents the UVB arm of X-shooter while the green region is VIS. Grey regions represents sections of the X-shooter spectra with bad pixels. SP013 in both panels are smoothed with a median filter with a 11 pixel window, while the other lines are smoothed with a 31 pixel window.

### *4.2. BLR geometry*

The difference in peak offset between H (close to systematic redshift) and He (almost 100 km s$^{-1}$ blueshifted) indicates a stratified BLR, while the larger FWHM in He I indicates that He is at a smaller radial distance. This is consistent with the theory (Korista & Goad 2004) and observations from velocity-resolved reverberation mapping (e.g., Kollatschny 2003; Bentz et al. 2010). However, the large uncertainty associated with He I (see Table B.1) makes it impossible to meaningfully conclude the BLR geometry based on this information.

The kinematics of the Balmer lines were well measured and so was the velocity offset of the redshifted O I line. The latter implies the presence of an inflow. We know that this jetted source is observed face on, with a viewing angle of <50 deg, as constrained by Schulz et al. (2016). Therefore, under a disk-wind model, for Balmer lines to not have a significant peak offset implies the emitting region is moving perpendicular to the line of sight. Building on this assumption, two scenarios exist for placing the other emitting regions. The first is a single stream of material that follows the locally optimally emitting clouds (LOC, Baldwin et al. 1995) model, with He I, Paschen, and Balmer lines, ending with O I. This implies a greater push at the start of the stream, thus the blueshifted peaks of He I. The second is a dual-stream disk model (e.g., Yong et al. 2017) with He wind radially closer and at a higher inclination than the H wind, not placing Oi inflow at any required position. Reverberation mapping will be needed to fully investigate the structure, and a higher resolution spectrum with better S/N focusing on the Paschen, He I, and He II lines is required.

Our results reveal perplexing line fluxes and ratios. The Balmer decrement is very steep at H$\alpha$:H$\beta$:H$\gamma$:H$\delta$ = 4.67:1.00:0.31:0.15. Also, Pa$\alpha$/Pa$\beta$ = 1.08, but Pa$\alpha$/H$\beta$ = 0.50 is very low (all values were derived from the fluxes presented in Table B.1). A reddening effect does not explain this as a consistent range of case B values for H$\gamma$/H$\beta$ would worsen

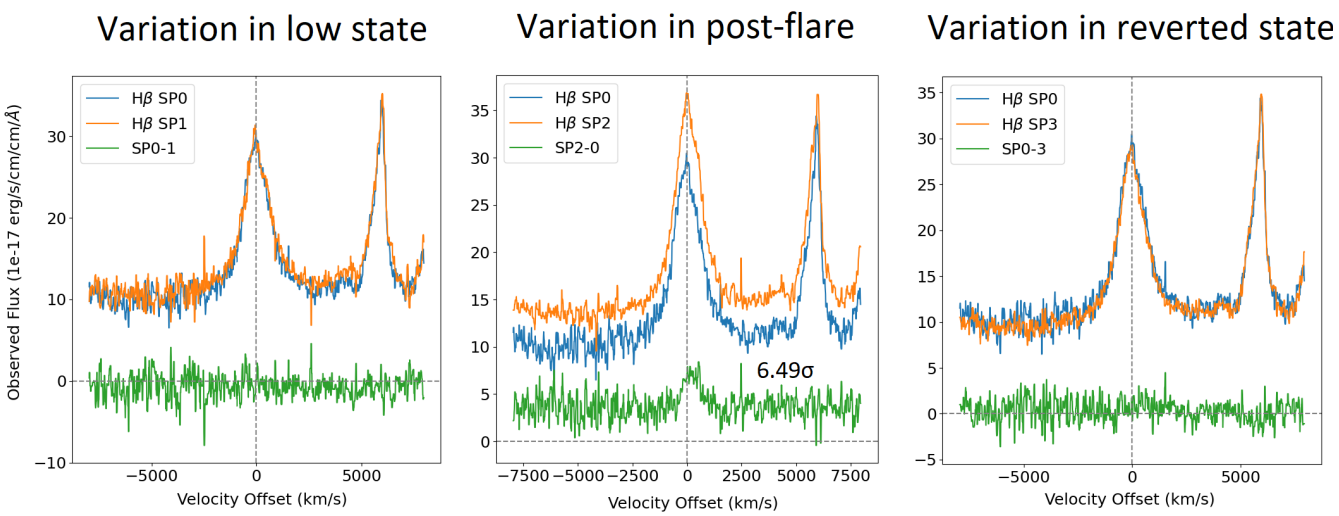


**Fig. 3.** Variation of the H$\beta$ region in the low-state, post-flare and reverted-state. All lines are smoothed with a median filter with a 5 pixel window, which is much much narrower than any features that could be present. In each panel, a relevant spectrum, shown in orange, is subtracted against SP0, which is acting as the baseline in these plots and shown in blue. Their subtracted result is shown in green. The observed flux is the $y$-axis and velocity offset is $x$-axis. We also indicate the 0 value in the $y$- and $x$- axes for every panel with vertical and horizontal dashed lines. These visual aids emphasise the non-zero redshift in the emission line excess in H$\beta$ during the post-flare. The statistical significance of the excess is also given in the relevant panels, see footnote 3 for details. We see that the green line in the low-state and reverted-state are consistent with 0, indicating no broad-line variation outside of the flare. This figure is a truncated version of Fig. B.2.

the Pa$\alpha$/H$\beta$ ratio and result in H$\alpha$/H$\beta$ being too low. A differential in optical depth could explain the Balmer ratios, yet this would require an unusually high optical depth of $\gg$1000 (see Fig. 9 of Davidson & Netzer 1979). Balmer line ratios are known to be correlated with a velocity offset, where the H$\alpha$/H$\beta$ increases towards the peak of a line profile (Stirpe 1991). This could be a feasible explanation as the line profile observed in PKS 2004−447 is highly dominated by the peak. Alternatively, the emission lines may not be completely recombination driven, and a partial local thermodynamical equilibrium exists and the Saha-Boltzmann relations hold for part of the BLR (Popović 2003). This is supported by the Balmer ratios in PKS 2004−447 being similar to 3C 390.3 and 3C 382 from that work.

### 4.3. Understanding of red excess

The red excess and the flare are correlated events. This is the first observed event where a $\gamma$-ray flare is associated with a local change in the BLR with distinct kinematic properties. If multiple spectra were taken as soon as the flare started, we could assess if the red excess appeared before or after the flare. If they were taken before, we would observe the red excess fading, implying a link to the cause of flare. If they were taken after, we would see the excess grow, suggesting a direct contribution of the jet to the red excess.

The most curious aspect of the red excess is that it is redshifted. Here we speculate about four possible scenarios on how it is formed. All of the speculated scenarios would be extremely interesting to study, and we encourage frequent observation immediately after a flare for all $\gamma$-NLS1s.

(1) The simplest scenario is a bipolar outflow, with receding gas visible and approaching gas partially obscured. This is motivated by the red excess being more prominent towards the blue and absent for the IR Paschen lines. The O I inflow also supports this model. The flare would reverberate throughout both flows equally, reaching most of the material within a month. However, shorter wavelength emissions from the approaching ions would be obscured, biasing a redward enhancement.

(2) The $\gamma$-ray flare directly creates the red excess. If the event occurred above the H and He emitting region, a shock wave from the event would push the gas down, introducing more material into the emitting region. In this scenario, we should also observe red excesses in Mg II and O I, but that is not seen. This is a point of contention for this scenario. Using the BLR radius calculated by Berton et al. (2021) of ∼15 light days, a $FWHM \sim 1500\,\mathrm{km\,s^{-1}}$, and assuming $t_{\rm dyn} \approx R_{\rm BLR}/FWHM$ gives a dynamical timescale of 8 years. This is the time needed for the introduced material to re-equilibrate, which is longer than the 1.5 years between SP2 and SP3. Reconciling this requires that the event occurred at a distance <3 light days, which is consistent with the predicted location of $\gamma$-ray production at $\sim 10^3 r_{\rm g} \sim 1$ light day (Ghisellini et al. 2010).

(3) The flaring event led to an increased illumination onto a region close enough to the black hole to experience strong gravitational redshift. A shift of $250\,\mathrm{km\,s^{-1}}$ yields an emitting radius of ∼1 light day (with $M_{\rm bh} = 1.5 \times 10^7\,M_\odot$ from Berton et al. 2021), which is consistent with an increased illumination from the $\gamma$-ray flare itself. The emergence of the red excess should be instant due to its proximity to the black hole and $\gamma$-ray source. However, its visibility a month after the flare poses an issue, even accounting for gravitational time dilation.

(4) The accretion disk or BLR undergo a structural change that leads to the flare and increased illumination in a specific part of the BLR. This region could be close to or far from the black hole. If it is close, the duration of the illumination is not tied to the short-lived flare unlike in scenario (3). If it is far, since O I is an established inflow, that might imply the outermost parts of the BLR are always infalling. This region might contribute to part of the red wing observed in the permitted line profiles, which can be verified with velocity-resolved reverberation mapping. The relevant timescale for this interaction is not well understood, as the infalling timescale based on the viscosity parameter

has been shown to be flawed as demonstrated by changing-look AGN (Lawrence 2018).

*Acknowledgements.* We appreciate the effort and time of the anonymous referee in improving on this manuscript. W.-J.H., M.B., and E.S. acknowledge the support of the ESO studentship programme. M.B. and E.C. are ESO fellows. E.C. acknowledges support from ANID project Basal AFB-170002. Based on observations collected at the European Southern Observatory under ESO programmes 099.B-0785 and 104.20UC. A.R.L. acknowledges the support by FONDECYT Postdoctorado project No. 3210157.

## References

Abdo, A., Ackermann, M., Ajello, M., et al. 2009, ApJ, 707, L142
An, T., Lao, B.-Q., Zhao, W., et al. 2017, MNRAS, 466, 952
Baldwin, J., Ferland, G., Korista, K., & Verner, D. 1995, ApJ, 455, L119
Barbary, K. 2016, J. Open Source Softw., 1, 58
Bentz, M. C., Walsh, J. L., Barth, A. J., et al. 2010, ApJ, 716, 993
Bertin, E., & Arnouts, S. 1996, A&AS, 117, 393
Berton, M., Caccianiga, A., Foschini, L., et al. 2016, A&A, 591, A98
Berton, M., Foschini, L., Caccianiga, A., et al. 2017, Front. Astron. Space Sci., 4, 8
Berton, M., Peluso, G., Marziani, P., et al. 2021, A&A, 654, A125
Boller, T., Brandt, W., & Fink, H. 1996, A&A, 305, 53
Bon, E., Gavrilović, N., La Mura, G., & Popović, L. 2009, New Astron. Rev., 53, 121
Boroson, T. A., & Green, R. F. 1992, ApJS, 80, 109
Brown, A. G., Vallenari, A., Prusti, T., et al. 2021, A&A, 649, A1
Chen, S., Berton, M., La Mura, G., et al. 2018, A&A, 615, A167
Choi, H., Leighly, K. M., Terndrup, D. M., Gallagher, S. C., & Richards, G. T. 2020, ApJ, 891, 53
Cracco, V., Ciroi, S., Berton, M., et al. 2016, MNRAS, 462, 1256
D'Ammando, F., Orienti, M., Finke, J., et al. 2013, MNRAS, 436, 191
Davidson, K., & Netzer, H. 1979, Rev. Mod. Phys., 51, 715
Denney, K., Peterson, B. M., Pogge, R., et al. 2009, ApJ, 704, L80
Done, C., & Krolik, J. H. 1996, ApJ, 463, 144
Fitzpatrick, E. L. 1999, PASP, 111, 63
Foschini, L. 2020, Universe, 6, 136
Foschini, L., Angelakis, E., Fuhrmann, L., et al. 2012, A&A, 548, A106
Foschini, L., Berton, M., Caccianiga, A., et al. 2015, A&A, 575, A13
Gallo, L., Edwards, P., Ferrero, E., et al. 2006, MNRAS, 370, 245
Ge, X., Zhao, B.-X., Bian, W.-H., & Frederick, G. R. 2019, ApJ, 157, 148
Ghisellini, G., Tavecchio, F., Foschini, L., et al. 2010, MNRAS, 402, 497
Gokus, A., Paliya, V., Wagner, S., et al. 2021, A&A, 649, A77
Grupe, D. 2000, New Astron. Rev., 44, 455
Guo, H., Shen, Y., & Wang, S. 2018, Astrophysics Source Code Library [record ascl:1809.008]
Hamann, F., Korista, K. T., & Morris, S. L. 1993, ApJ, 415, 541
Harrison, C., Costa, T., Tadhunter, C., et al. 2018, Nat. Astron., 2, 198
Hopkins, P. F., & Elvis, M. 2010, MNRAS, 401, 7
Itoh, R., Tanaka, Y. T., Fukazawa, Y., et al. 2013, ApJ, 775, L26
Kausch, W., Noll, S., Smette, A., et al. 2015, A&A, 576, A78
King, A., & Pounds, K. 2015, ARA&A, 53, 115
Kollatschny, W. 2003, A&A, 407, 461
Komossa, S. 2008, Rev. Mex. Astron. Astrofis. Conf. Ser., 32, 86
Komossa, S., Voges, W., Xu, D., et al. 2006, AJ, 132, 531
Korista, K. T., & Goad, M. R. 2004, AJ, 606, 749
Kotilainen, J. K., León-Tavares, J., Olguín-Iglesias, A., et al. 2016, ApJ, 832, 157
Kreikenbohm, A., Schulz, R., Kadler, M., et al. 2016, A&A, 585, A91
Kron, R. G. 1980, ApJS, 43, 305
Lawrence, A. 2018, Nat. Astron., 2, 102
Leighly, K., & Casebeer, D. 2007, The Central Engine of Active Galactic Nuclei, 373, 365
Lenz, D. D., Newberg, J., Rosner, R., Richards, G. T., & Stoughton, C. 1998, ApJS, 119, 121
Lister, M. L., Aller, M., Aller, H., et al. 2016, AJ, 152, 12
Liu, H., Wang, J., Mao, Y., & Wei, J. 2010, ApJ, 715, L113
Mathews, W., & Capriotti, E. 1985, Astrophysics of Active Galaxies and Quasi-Stellar Objects (Univ Science Books), 185
Mathur, S. 2000, MNRAS, 314, L17
Maune, J. D., Miller, H. R., & Eggen, J. R. 2012, ApJ, 762, 124
Paliya, V. S., Stalin, C., Kumar, B., et al. 2013, MNRAS, 428, 2450
Peterson, B., McHardy, I., Wilkes, B. J., et al. 2000, ApJ, 542, 161
Peterson, B. M., Ferrarese, L., Gilbert, K., et al. 2004, ApJ, 613, 682
Popović, L. Č. 2003, ApJ, 599, 140
Rakshit, S., Stalin, C., Chand, H., & Zhang, X.-G. 2017, ApJS, 229, 39
Rodrigo, C., & Solano, E. 2020, XIV. 0 Scientific Meeting (virtual) of the Spanish Astronomical Society, 182
Rogerson, J. A., Hall, P. B., Rodríguez Hidalgo, P., et al. 2016, MNRAS, 457, 405
Scannapieco, E., & Oh, S. P. 2004, ApJ, 608, 62
Schlafly, E. F., & Finkbeiner, D. P. 2011, ApJ, 737, 103
Schulz, R., Kreikenbohm, A., Kadler, M., et al. 2016, A&A, 588, A146
Seyfert, C. K. 1943, ApJ, 97, 28
Shapovalova, A., Popović, L., Bochkarev, N., et al. 2009, New Astron. Rev., 53, 191
Smette, A., Sana, H., Noll, S., et al. 2015, A&A, 576, A77
Stirpe, G. 1991, A&A, 247, 3
Sulentic, J., Zwitter, T., Marziani, P., & Dultzin-Hacyan, D. 2000, ApJ, 536, L5
Tonry, J., Stubbs, C. W., Lykke, K. R., et al. 2012, ApJ, 750, 99
Trump, J. R., Hall, P. B., Reichard, T. A., et al. 2006, ApJS, 165, 1
Wanders, I., Goad, M. R., Korista, K. T., et al. 1995, ApJ, 453, L87
Williams, P. R., Pancoast, A., Treu, T., et al. 2018, ApJ, 866, 75
Yao, S., & Komossa, S. 2021, MNRAS, 501, 1384
Yong, S. Y., Webster, R. L., King, A. L., et al. 2017, PASA, 34, e042
Zubovas, K., & Nayakshin, S. 2014, MNRAS, 440, 2625

## Appendix A: Flux calibration from acquisition images

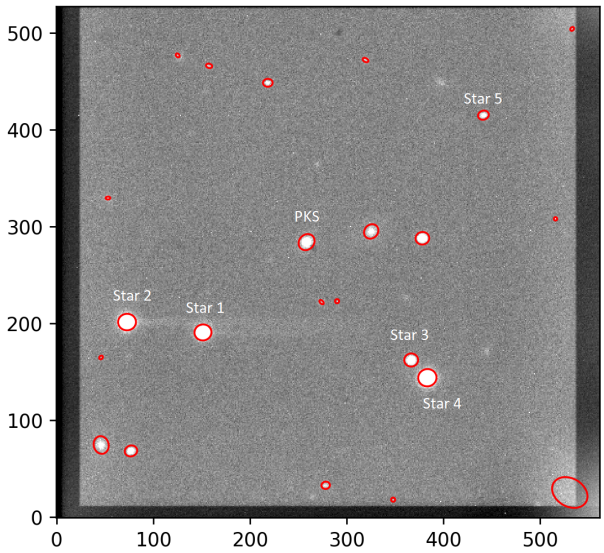


**Fig. A.1.** Acquisition image from SP0 with the sources selected by SEP marked in red ellipses. While there is a large number of false selections, we are only concerned with the ones that are labelled.

The final flux calibration of the spectra utilised the raw acquisition images taken under the *r*-band Sloan filter (Lenz et al. 1998). We calibrated these images by tweaking the zero point such that stars in the field (see Figure A.1), identified using Gaia's proper motion data (Brown et al. 2021, Gaia EDR3 data were used), had a constant magnitude across all observations. The baseline magnitude was taken from the Panoramic Survey Telescope and Rapid Response System (Pan-STARRS Tonry et al. 2012), which operates with a similar filter set. To measure star brightness, we used the python package for source extraction and photometry (Barbary 2016, SEP), a python version of Source Extractor (Bertin & Arnouts 1996). We focused on PKS 2004-447 and the five stars that are labelled. The fluxes were then counted from 2.5× the kron radius, resulting in the MAG_AUTO of Source Extractor. The kron radius is the first moment of the surface brightness light profile and sufficient amount of the total flux is contained within 2.5× this radius (Kron 1980).

**Table A.1.** List of measured photometry of objects in the PKS 2004-447 field across the four acquisition images.

| Object | SP0 | SP1 | SP2 | SP3 |
|---|---|---|---|---|
| ZP | 29.015 | 29.077 | 29.75 | 29.76 |
| PKS | 18.448 | 18.457 | 18.188 | 18.528 |
| Star 1 | 16.650 | 16.650 | 16.649 | 16.653 |
| Star 2 | 16.005 | 16.001 | 16.013 | 16.008 |
| Star 3 | 15.940 | 15.925 | 15.940 | 15.921 |
| Star 4 | 18.667 | 18.626 | 18.664 | 18.679 |
| Star 5 | 20.203 | 20.114 | 20.129 | 20.029 |

**Notes.** Columns: (1) object label; and (2-5) SDSS R-band magnitudes, with zero points (ZP) defined in the table of the objects in acquisition images associated with SP0, SP1, SP2, and SP3, respectively. Errors are not given as they are < 0.1% from Source Extractor, but the larger uncertainty comes from variations between epochs.

The zero points of each epoch were tweaked such that 'Star 1' remained almost constant at 16.650 magnitude. The other stars were then only variable of the order of 0.01 magnitude. 'Star 5' being much dimmer is an exception with variability of the order of 0.1 magnitude. This choice of zero points implies that PKS2004-447 has minimal variability between SP0 and SP1, and that it is at the brightest at SP2 and dimmest at SP3 for a maximum variation of 0.34 magnitude.

Assuming an AB magnitude, we converted PKS 2004-447 magnitudes into average fluxes across the Sloan Digital Sky Survey (SDSS) R band with information from the Spanish Virtual Observatory Filter Profile Service (Rodrigo & Solano 2020). Finally, we scaled the spectra of each epoch to match this derived flux level. We note that this process has converted slit continuum flux to kron aperture continuum flux to allow for comparison or variability between epochs without worrying about airmass losses or calibration uncertainties. This results in the emission lines' fluxes to be relatively accurate across epochs, but over-estimated by themselves with an average factor of 1.61. By undoing the scaling, we will recover the line luminosities when required. Also, slit differences between narrow emission lines have still not been accounted for. The full X-Shooter view of this source is shown in Figure A.2

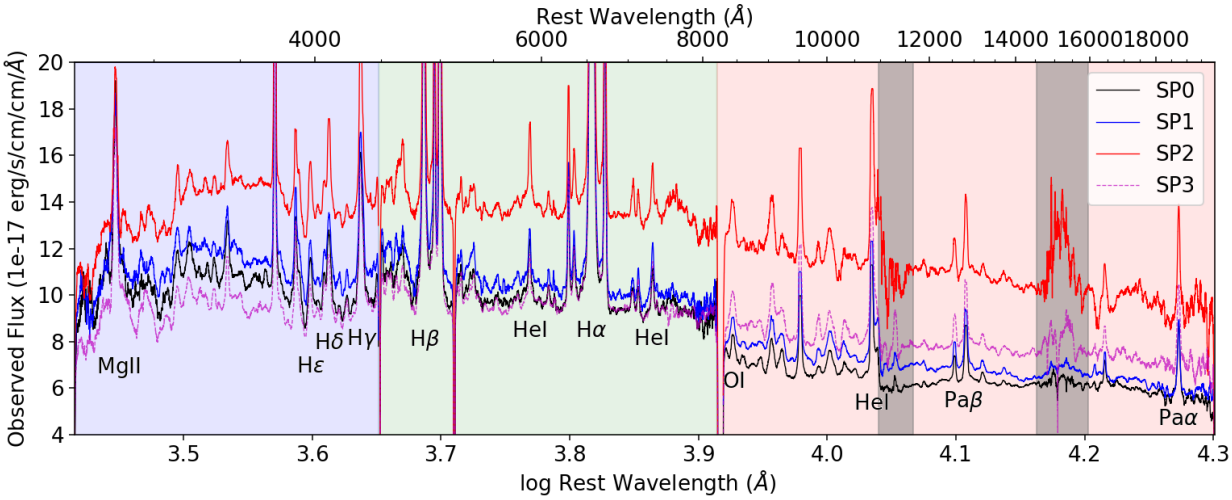


**Fig. A.2.** Full rest-frame wavelength range of SP0, SP1, SP2, and SP3. The colour sections indicate the three arms, while the two grey sections in the NIR arm mark the most problematic telluric regions that Molecfit was not able to recover.

## Appendix B: Spectral analysis and line fitting

We used the python script PyQSOFit by Guo et al. (2018) that utilises the least squares fitting package KMPFIT. The residuals were weighted based on the variance spectra. PyQSOFit has the functionality to fit a continuum and lines. For continuum fitting, while optimising the fitting range to feasibility, we approximated the rest-frame range from 3300-7500Å. This encompasses half of the UVB and the entire VIS arm. We fitted, with a free power law, a third-order polynomial, and the Fe II template from Boroson & Green (1992). The NIR arm was fitted separately and can be approximated by a power law in its entirely.

For line fitting, we used a modified version of PyQSOFit called PyQSOFit_SBL[5]. This version allows for skewed Gaussian and Voigt profile fitting. It also has the functionality to link the parameters of an unlimited number of fitted components. This reduced the degree of arbitrariness as we de-blended the H$\alpha$ line. It also reduced the number of individual parameters to vary per fitting, as well as increased the sampling of the parameter of each related component for a more accurate result. While the script is able to perform bootstrapping for error estimation, the more realistic errors would be from the variance of each measured value throughout the three spectra for the SP013.

One key finding through trial and error is that the forbidden lines need to be fitted with three components. These are a broad skewed Voigt for the outflows, a narrow skewed Gaussian intermediate component (NLR A), and a very narrow Gaussian component with very little offset relative to the host galaxy (NLR B). The NLR A and NLR B components are defined from [O III]$\lambda$5007; however, the broad component is different for every line. Either coincidentally, or physically, the narrow components of the permitted lines can be associated with NLR A and NLR B, so these were used to simplify the fitting procedure. The line profiles are subsequently described here and are also shown in Figure B.1, including [O III], and the results of the fitting is summarised in Table B.1.

**Balmer lines** - In the SP013 spectrum, the broad component of H$\delta$, H$\gamma$, and H$\beta$ are similar. In particular, H$\gamma$ and H$\beta$ have a detectable NLR A component. Furthermore, H$\gamma$ fitting is considered problematic as it is heavily blended with [O III]$\lambda$4363 and the continuum approximation over-subtracts the blue wing.

We note that H$\alpha$ is complicated as it is directly blended with [N II], and potentially blended with He I$\lambda$6678 and [S II] on the red wing. The final fitting to measure H$\alpha$ broad emission lines used a total of seven components; four for the [N II] doublet with two NLR A and two broad components set to the theoretical ratio; three for H$\alpha$ with NLR A, NLR B, and a broad component that is associated with H$\beta$ (not fixed, but has to be similar). The blending from He I$\lambda$6678 and [S II] was not significant, and the final component of [N II] was comparatively too weak to alter the H$\alpha$ broad line.

**Paschen lines** - Paschen lines observed ranges from Pa$\epsilon$ to Pa$\alpha$; however, we have only been able to acquire reliable line-fitting measurements for Pa$\beta$ and Pa$\alpha$. We note that Pa$\epsilon$ is heavily blended with [S III]$\lambda$9531, and Pa$\delta$ and Pa$\gamma$ are both dominated by noise that was introduced by telluric absorption. We find a broad component and a NLR A component for both Pa$\beta$ and Pa$\alpha$. Broad Pa$\alpha$ is problematic due to telluric noise, causing an unreliable continuum definition.

**Helium lines** - Of the observed He lines, we could only reliably measure He I$\lambda$10830. The only He II line is at $\lambda$4686, but it sits in the region with heavy Fe II emission, which we were unable to constrain. We note that He I $\lambda$3889 and $\lambda$7065 are very weak; the former suffers from continuum definition issues and the latter suffers from profile blending from multiple lines. Furthermore, He I $\lambda$5876 has continuum definition issues, but we were able to acquire a reliable fit by assuming that it has the exact same profile as He I$\lambda$10830. Both He I $\lambda$5876 and $\lambda$10830 have a significant NLR A component.

**Red excess** All of the red excesses are fitted with a single non-skewed Gaussian component, with no width or offset constraints. The measurement for He I$\lambda$5876 was extremely problematic as the continuum is not well defined in that region, resulting in contamination from continuum variation. Also He I$\lambda$10830 suffers from contamination from telluric correction variation. As such, their widths and peak offsets are not as reliable as the Balmer lines. We also observed a red excess on He I$\lambda$6678, but this is heavily contaminated by [S II]$\lambda$6725 and H$\alpha$ variations. While not listed because of the inaccurate measurement, it is a significant red excess with a FWHM= 1765 ± 425 km s$^{-1}$, a redshift of 620±600 km s$^{-1}$, and a flux of 21.52±8.52 × 10$^{-17}$ erg/s/cm/cm.

[5] https://github.com/JackHon55/PyQSOFit_SBL

**Table B.1.** Summary of permitted lines observed and fitted, and the red excesses observed and fitted.

| Line | Wavelength (Å) | Comment | SP013 Spectrum FWHM (km/s) | Offset (km/s) | Kurtosis | Flux $10^{-17}$ (erg/s/cm$^2$) | Red excess FWHM (km/s) | Offset (km/s) | Flux $10^{-17}$ (erg/s/cm$^2$) |
|---|---|---|---|---|---|---|---|---|---|
| UVB With Major Continuum Issues | | | | | | | | | |
| Mg II | 2799.00 | Undef. Ctm | | | | | | | |
| He I | 3888.647 | Undef. Ctm | | | | | | | |
| H$\epsilon$ | 3970.079 | Undef. Ctm | | | | | | | |
| H$\delta$ | 4101.742 | | 1580 | 0 | -0.01 | 56.68 | 905 | 240 | 12.50 |
| | | | ±25 | 0 | 0 | ±5.07 | ±120 | ±50 | ±4.73 |
| H$\gamma$ | 4340.471 | Problematic | 1580 | 0 | 0.22 | 115.26 | 1030 | 285 | 25.37 |
| | | | ±25 | 0 | ±0.05 | ±2.21 | ±30 | ±35 | ±2.34 |
| VIS | | | | | | | | | |
| He II | 4685.710 | Undef. Ctm | | | | | | | |
| H$\beta$ | 4861.333 | | 1580 | 0 | -0.01 | 375.86 | 905 | 240 | 37.60 |
| | | | ±25 | 0 | 0 | ±7.06 | ±80 | ±40 | ±4.87 |
| He I | 5875.624 | Problematic | 1660 | −85 | 1.89 | 58.51 | 795 | 220 | 16.18 |
| | | | ±175 | ±40 | ±0.95 | ±8.48 | ±195 | ±85 | ±3.96 |
| H$\alpha$ | 6562.819 | Blend | 1565 | 45 | 0 | 1755.63 | 1130 | 180 | 179.52 |
| | | | ±60 | ±35 | 0 | ±224.10 | ±200 | ±60 | ±65.6 |
| He I | 7065.196 | Problematic | | | | | 820 | 340 | 9.69 |
| | | | | | | | ±150 | ±20 | ±1.71 |
| NIR Few Telluric Issues | | | | | | | | | |
| O I | 8446.359 | Telluric | 1560 | 180 | 0 | 97.15 | | | |
| | | | ±225 | ±75 | 0 | ±13.58 | | | |
| Pa$\epsilon$ | 9545.969 | Blend | | | | | | | |
| Pa$\delta$ | 10049.368 | Telluric | | | | | | | |
| He I | 10830.340 | | 1660 | −85 | 1.89 | 268.68 | 1320 | 150 | 103.06 |
| | | | ±175 | ±40 | ±0.95 | ±40.54 | ±155 | ±110 | ±35.09 |
| Pa$\gamma$ | 10938.086 | Telluric | | | | | | | |
| Pa$\beta$ | 12818.072 | | 1500 | 0 | 0 | 172.11 | 1100 | 25 | 30.97 |
| | | | ±60 | 0 | 0 | ±25.28 | ±70 | ±105 | ±12.26 |
| Pa$\alpha$ | 18750.976 | Telluric | 1550 | −25 | −0.7 | 186.14 | 760 | 35 | 37.01 |
| | | | ±225 | ±70 | ±0.58 | ±50.19 | ±180 | ±95 | ±20.66 |

**Notes.** Columns: (1) emission line name; (2) rest-frame wavelengths measured in air in Å; (3) specific comments regarding issues in line fitting the profile. Undef. Ctm refers to lines for which we are unable to accurately define the continuum for a fit. For telluric, problematic, and blend, refer to text in Appendix B; (4) FWHM of the line profile from SP013 in km/s, with empty entries indicating that the feature was not fitted; (5) velocity offset of the line profile from SP013 in km/s, with negative values indicating a blueshift; (6) kurtosis or skew of the line profile from SP013; (7) flux of the emission line from SP013 in $10^{-17}$ erg/s/cm/cm; (8) FWHM of the red excess in km/s; (9) velocity offset of the red excess in km/s; and (10) flux of the red excess in $10^{-17}$ erg/s/cm/cm.

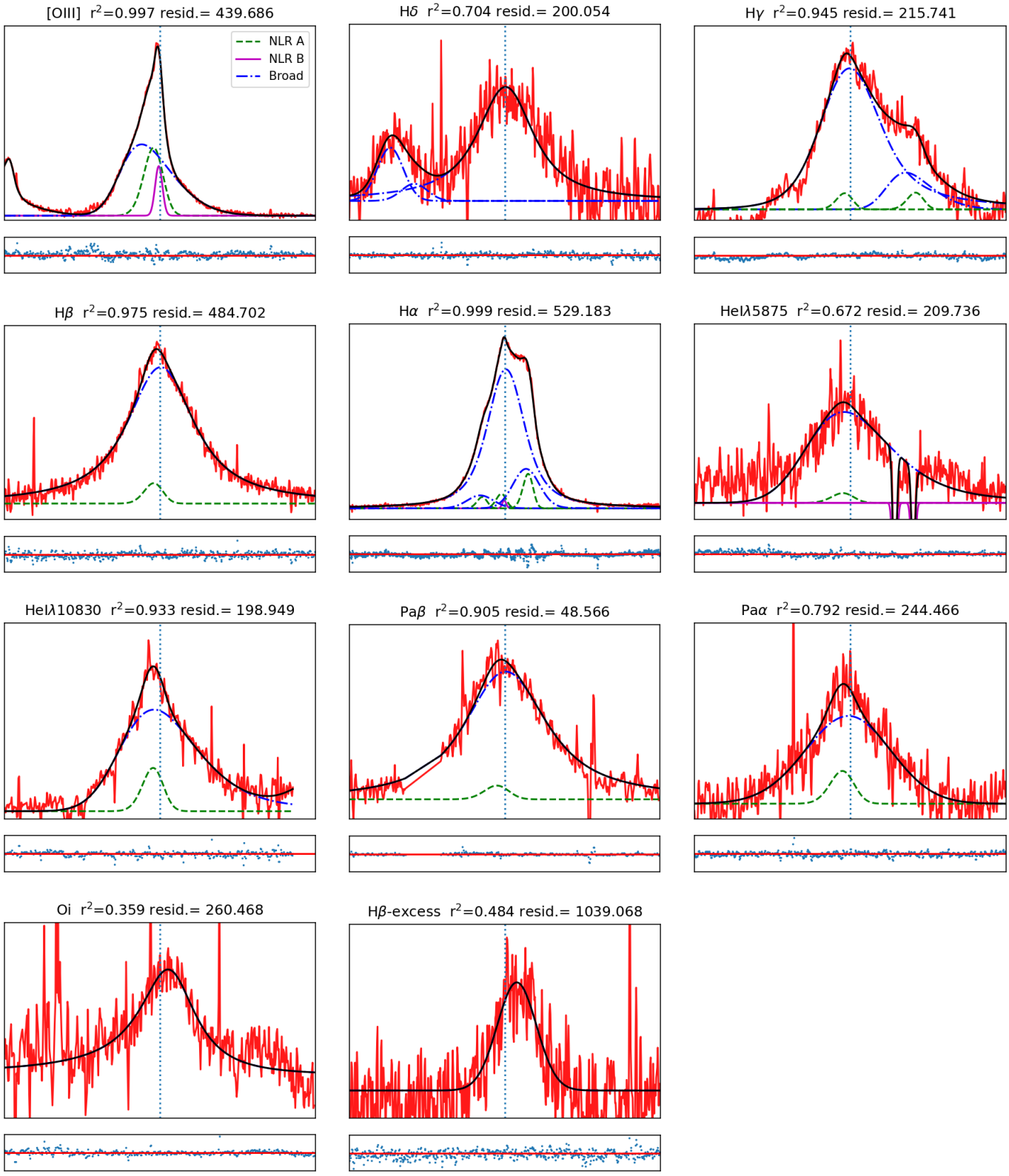


**Fig. B.1.** Line fitting on continuum subtracted SP013. Each panel has a top plot to show the components used to fit them, and a bottom plot to show the residuals. All lines are colour coded based on the legend of [O III]. The last plot shows the red-excess fitting for H$\beta$, which has the best and isolated signal. It is not conclusive if the feature can be approximated with a Gaussian.

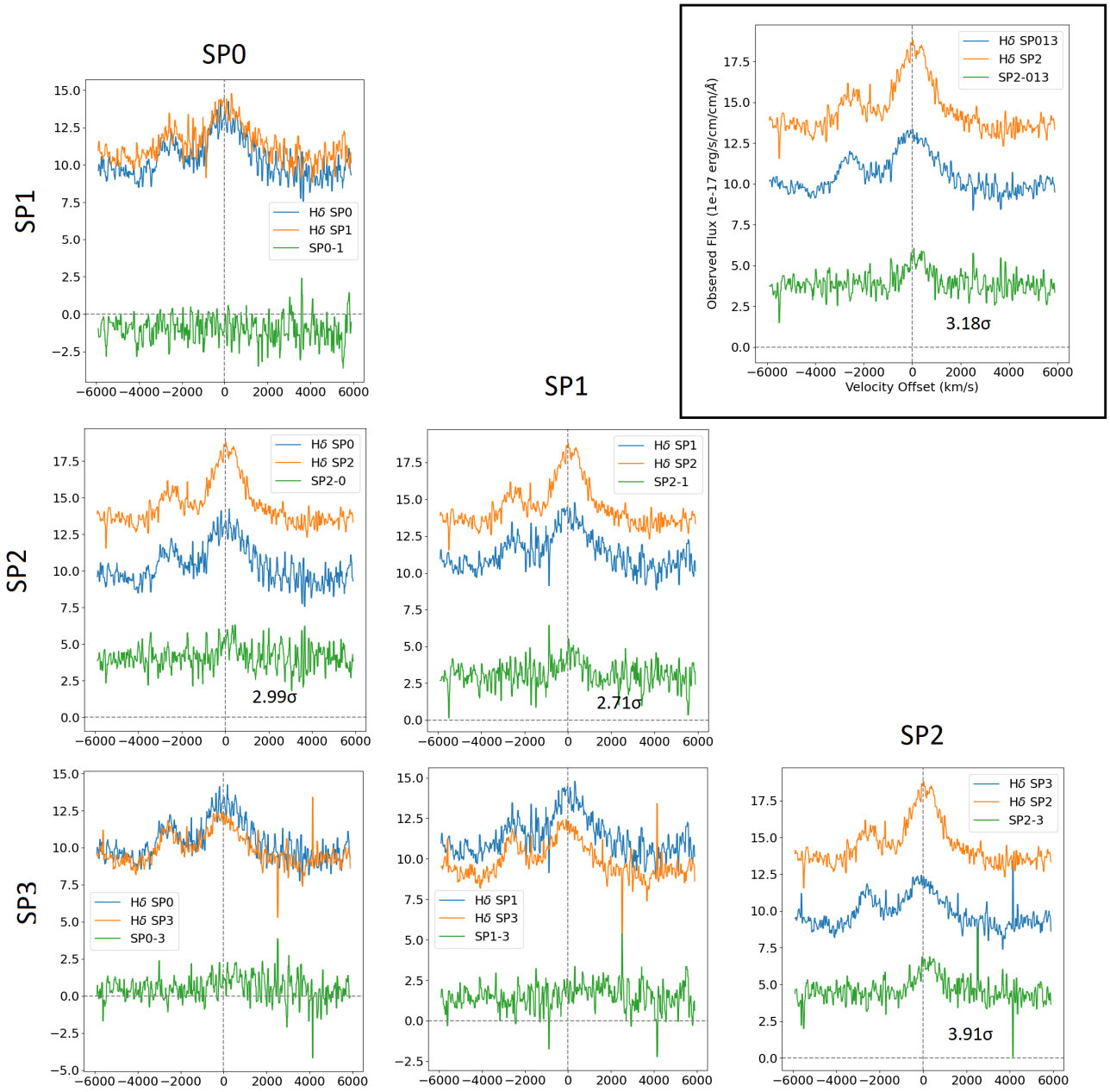


**Fig. B.2.** Full version of Figure 3, showing all of the lines with enhancements or red excesses. This is a grid of plots showing an emission line region from the four X-SHOOTER spectra. All lines have been smoothed with a median filter with a 5 pixel window, which is significantly narrower than any features that could be present. In each panel, two spectra (blue and orange line) and their subtracted result (green line) are plotted with the observed flux in the y-axis and the velocity offset in the x-axis. The two spectra in each panel are plotted depending on the row and column as indicated in large font. For example, the bottom right corner plots SP2 and SP3. In the top left corner, the panel with a black box plots SP013 and SP2. We also indicate the 0 value in the y- and x- axes for every panel with vertical and horizontal dashed lines. These visual aids emphasise the non-zero redshift in the emission line excess in panels involving SP2. The statistical significance of the excess is also given in the relevant panels (see footnote 3 for details). We see that in all other panels without SP2, the green line is consistent with 0, indicating almost no variation outside of the flare.

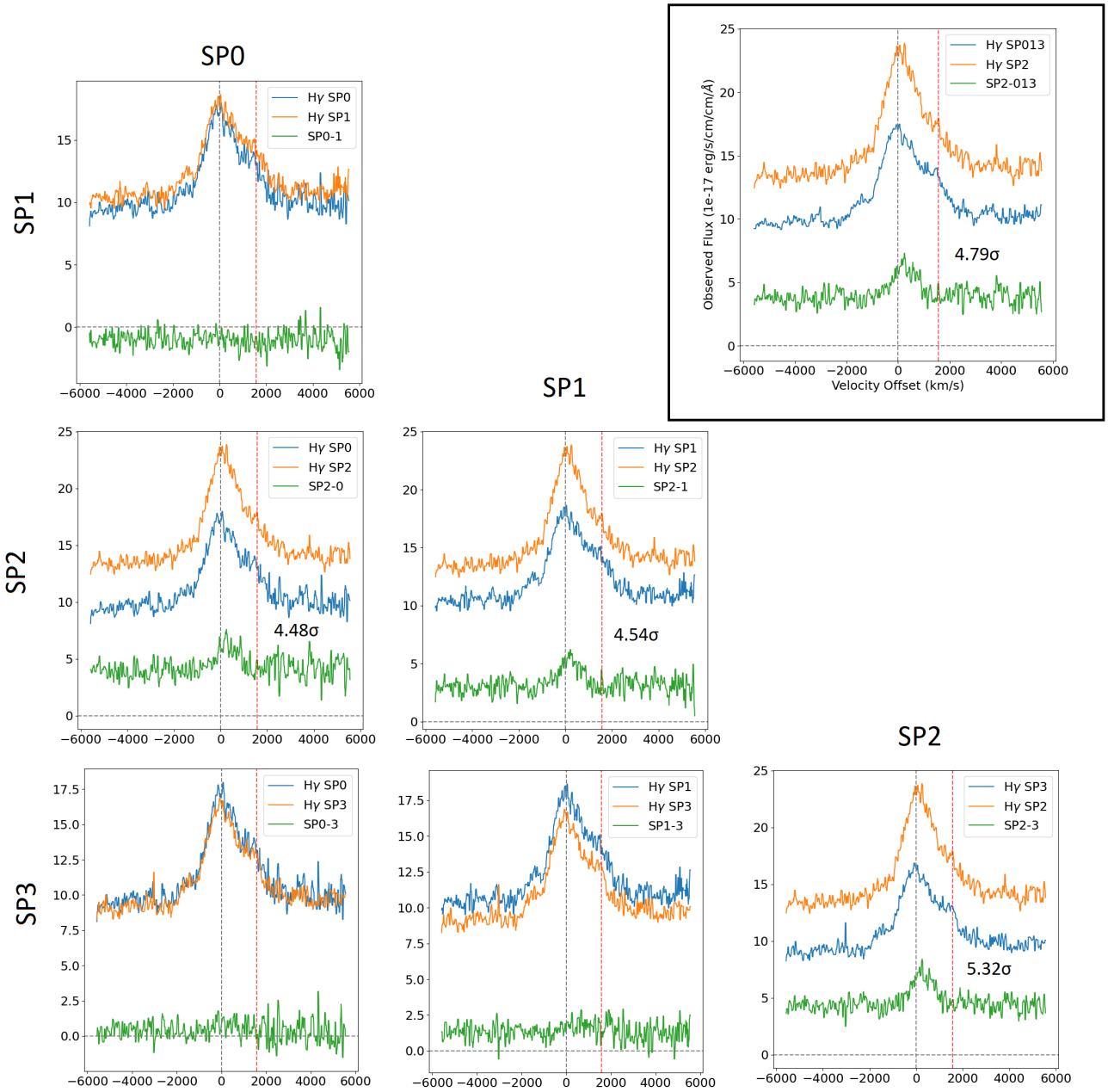


**Fig. B.2.** Continued. For the grid plots for H$\gamma$, the additional vertical red dashed line indicates the wavelength position of [O III]$\lambda$4364, and they appear to be properly cancelled in the subtracted line for all.

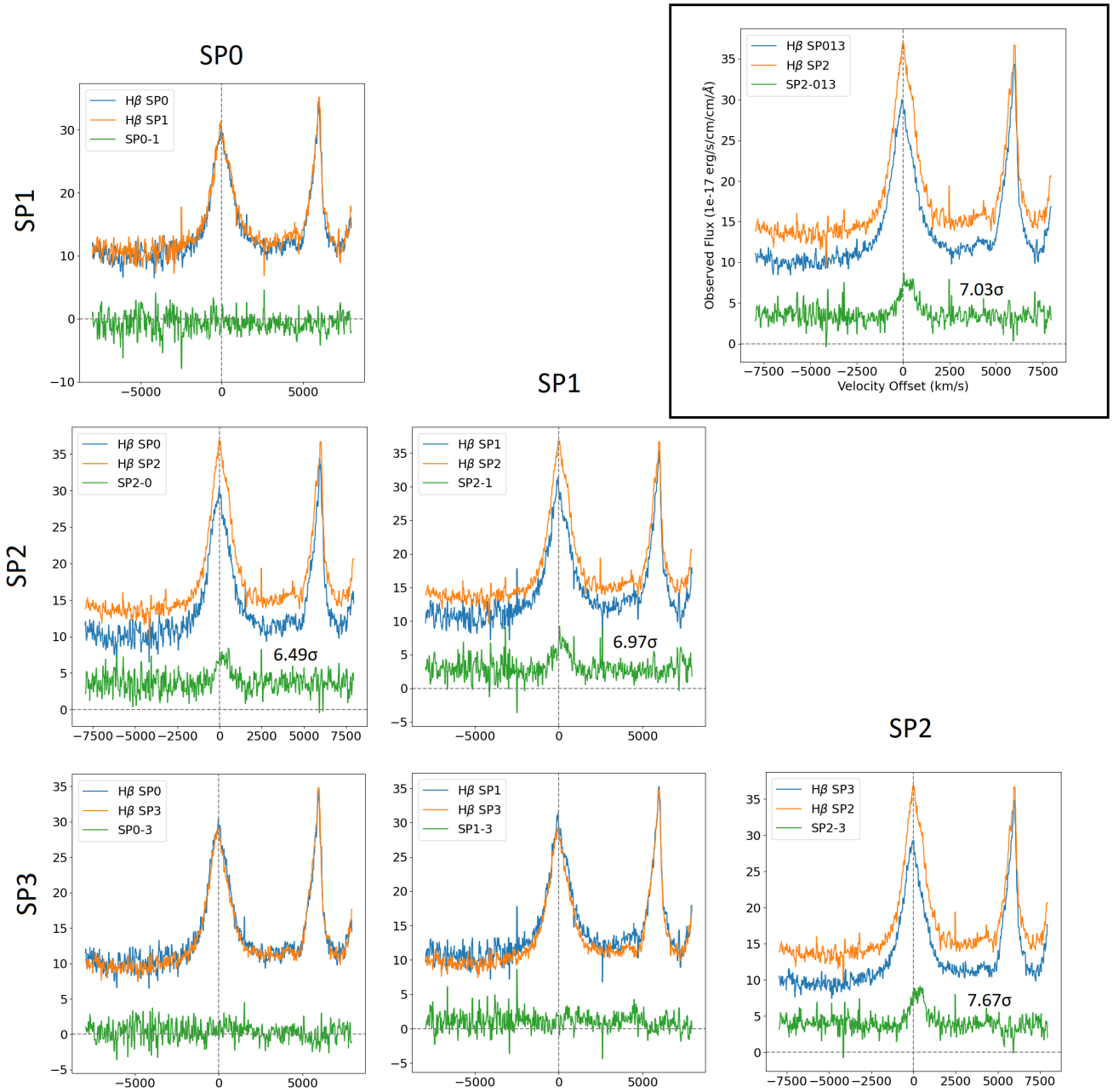


**Fig. B.2.** Continued.

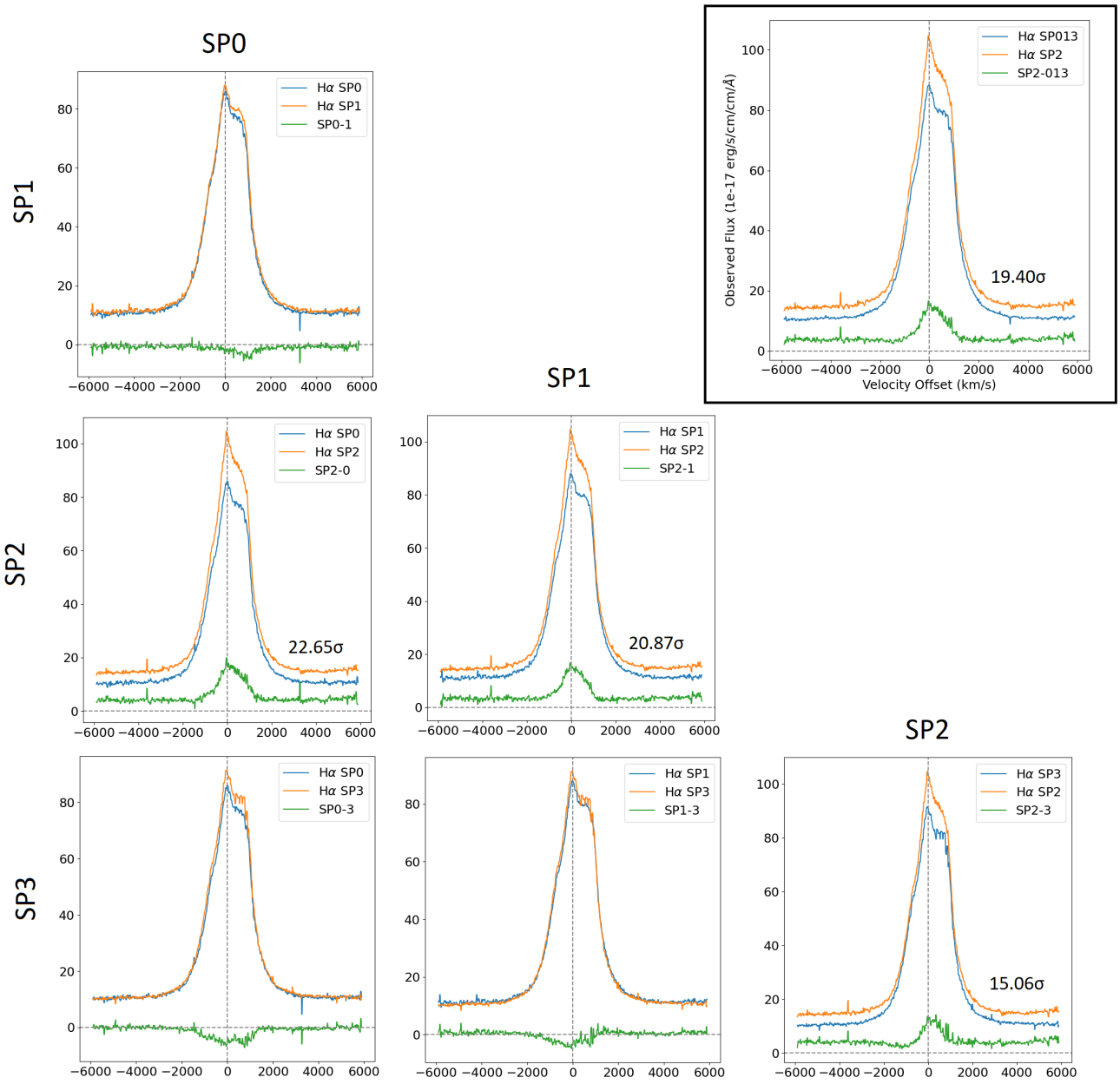


**Fig. B.2.** Continued.

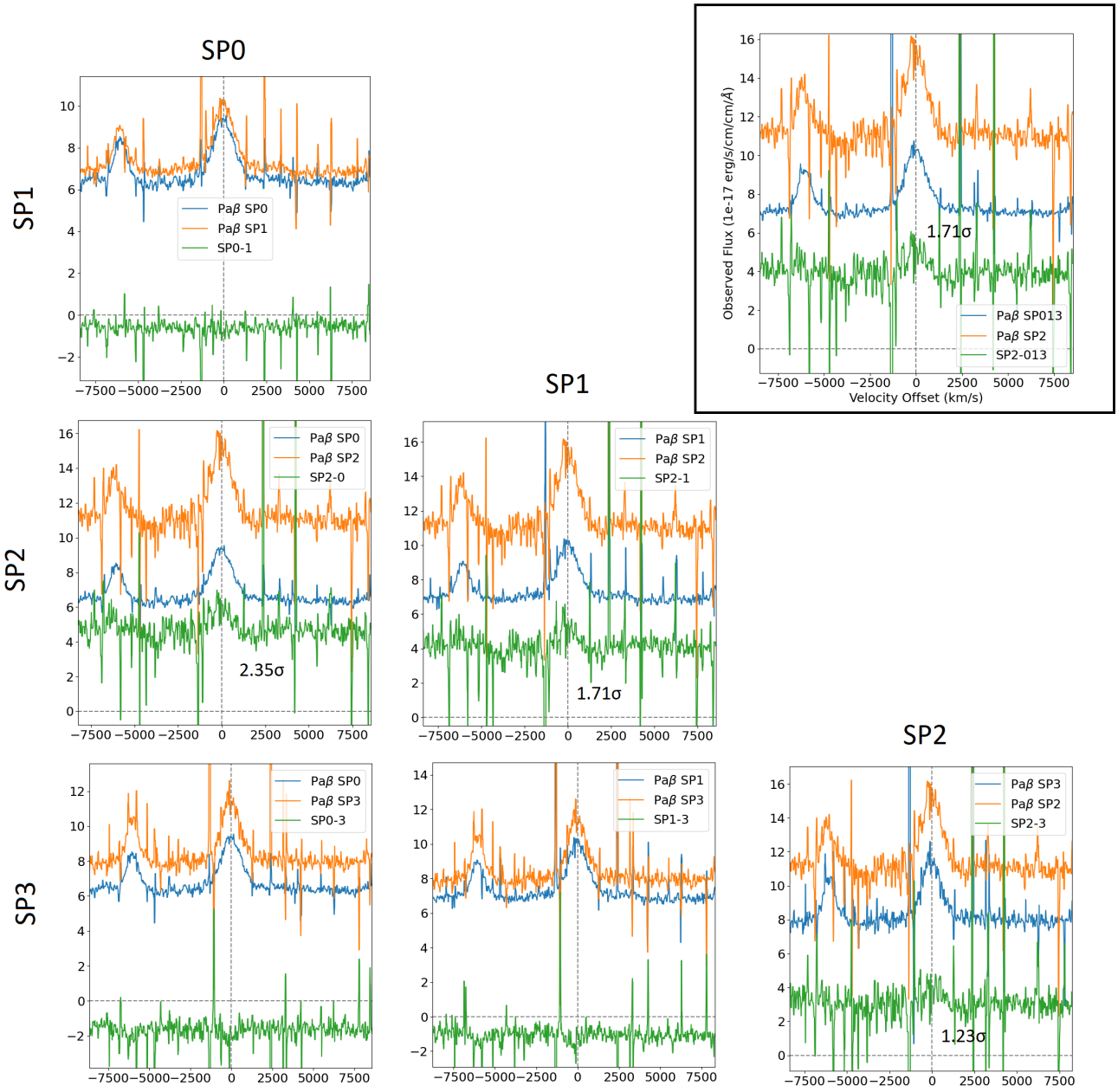


**Fig. B.2.** Continued. Statistical significance measured using RMS value taken from SP2 featureless continuum between 13000-13500Å.

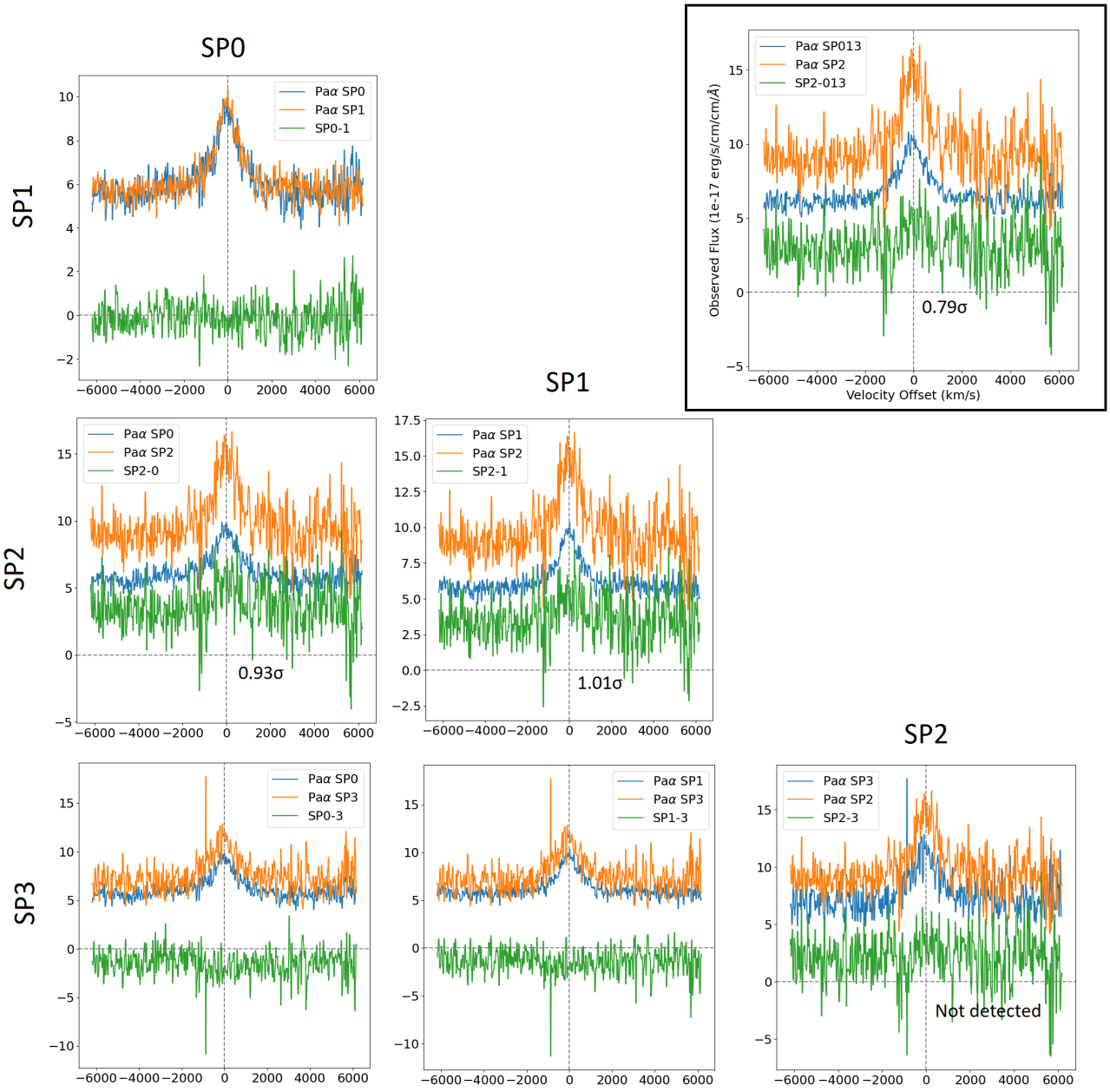


**Fig. B.2.** Continued. Statistical significance measured using RMS value taken from SP2 featureless continuum between 18000-18500Å. This is different to Pa$\beta$ as the quality from X-Shooter degrades towards the red end of the IR arm.

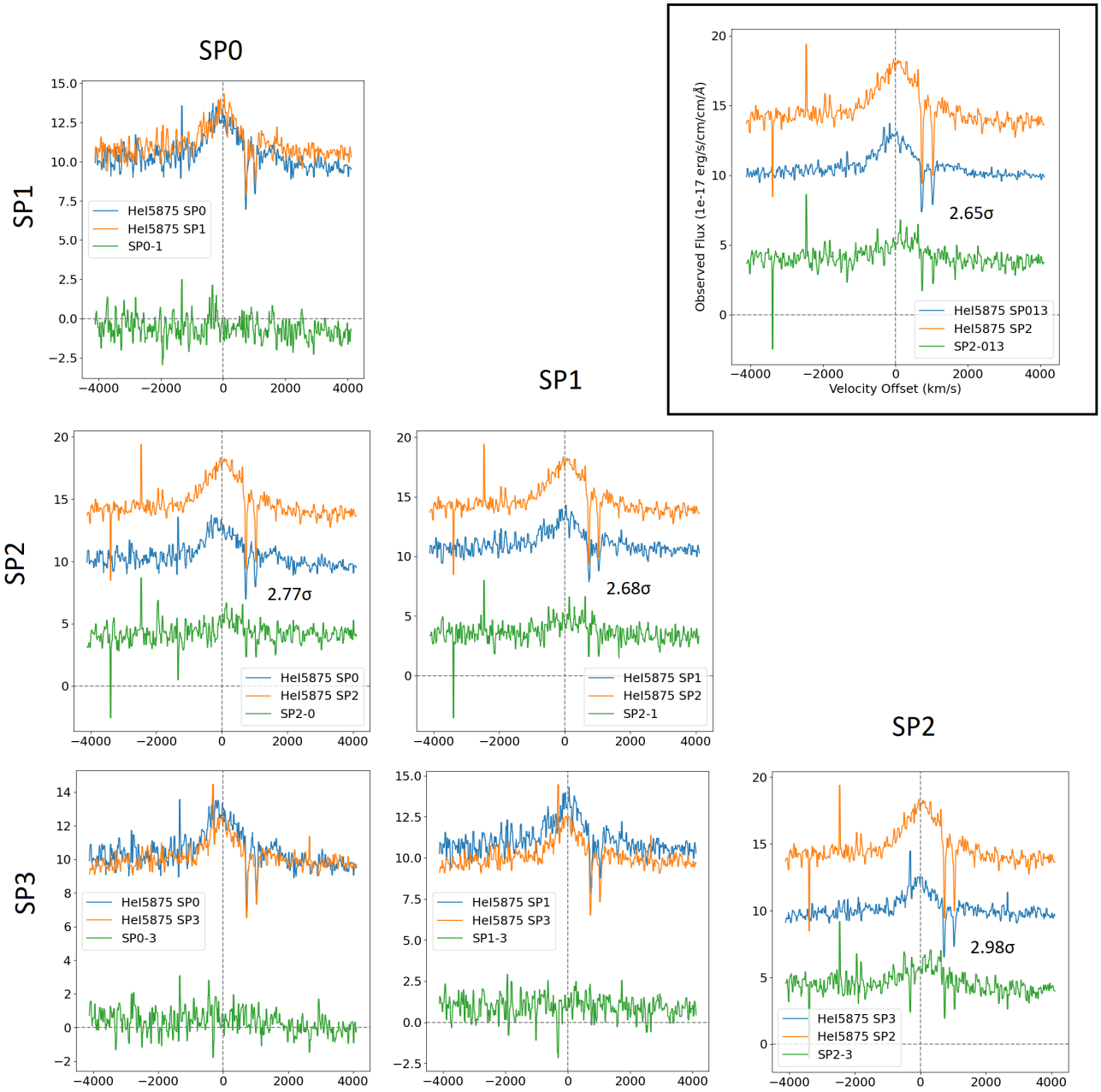


**Fig. B.2.** Continued.

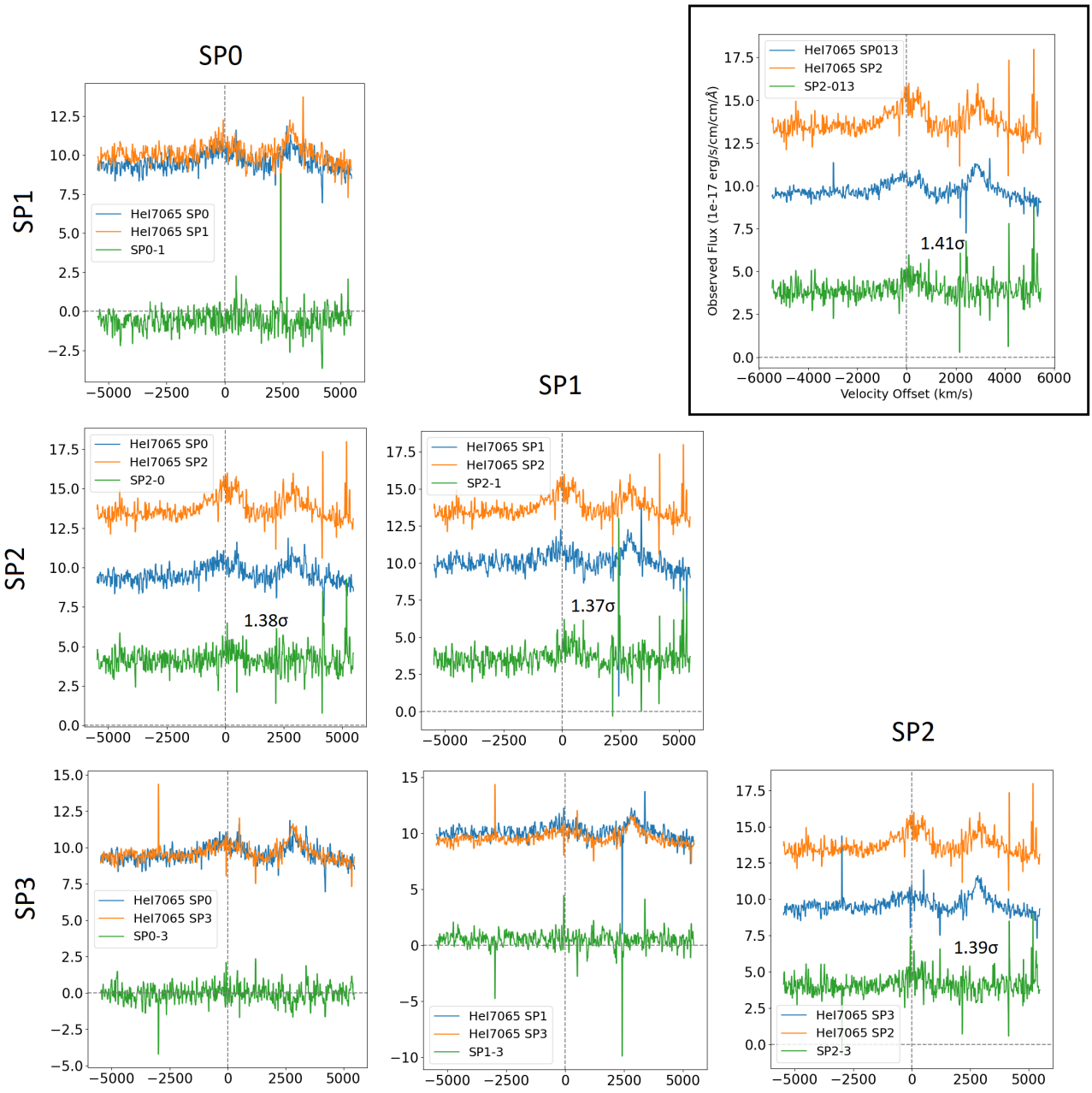


**Fig. B.2.** Continued.

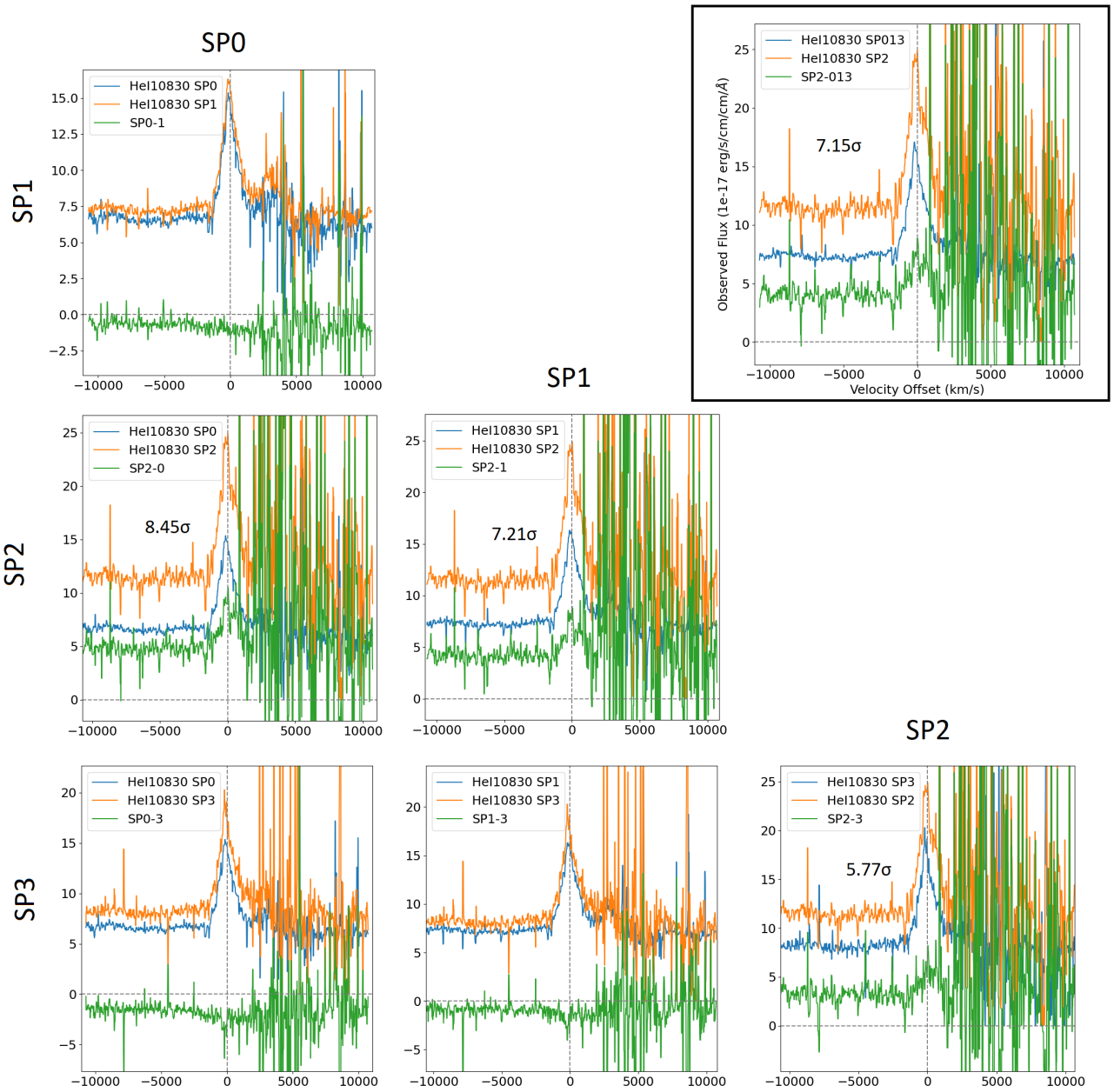


**Fig. B.2.** Continued. Statistical significance measured using RMS value taken from SP2 featureless continuum between 13000-13500Å.